

Influence of hexadecapole and hexacontatetrapole deformations and associated orientations on the synthesis of superheavy nuclei

Diksha[†] Harshit Sharma[‡] Manoj K. Sharma[§]

Department of Physics and Materials Science, Thapar Institute of Engineering & Technology, Patiala- 147004, Punjab, India

Abstract: The study examines the impact of higher-order deformations up to hexacontatetrapole (β_6) deformation on the synthesis of superheavy elements (SHN) through heavy-ion induced fusion reactions. The main objective of the study is to examine the impact of modified nuclear shapes, resulting from the collective influence of deformations (up to β_6), on the barrier characteristics V_B and R_B and overall dynamics of nuclear reactions leading to the synthesis of SHN. The analysis takes into account both spherical+deformed and deformed+deformed projectile-target (P-T) combinations, leading to the synthesis of SHN. Furthermore, the analysis also delves into the influence of the sign (\pm) and magnitude of β_6 on the barrier characteristics and overall reaction dynamics. This analysis examines these effects by utilizing ^{48}Ca , ^{36}S and ^{48}Ti induced reactions with β_6 -deformed actinide targets. The compact and elongated orientations, influenced by the sign and magnitude of β_2 , β_4 , and β_6 deformations, respectively, introduce further modifications in the reaction dynamics. The capture cross-sections (σ_{cap}), incorporating β_6 along with β_2 and β_4 deformation, result in a better alignment of the calculated cross-sections with the experimental data than the $\beta_2\beta_4$ deformations, due to modified barrier characteristics, particularly at near-barrier energies. The findings underscore the importance and impact of incorporating deformations (up to β_6) and their corresponding orientations to achieve a thorough understanding of the dynamics of heavy-ion induced reactions pertaining to the superheavy mass region.

Keywords: Nuclear Deformation, Nuclear Fusion, Superheavy Nuclei, Nuclear Reaction

DOI: **CSTR:**

I. INTRODUCTION

The investigation of the characteristics and synthesis of superheavy nuclei (SHN) has emerged as a prominent area of research in nuclear physics over the past few decades. The exploration of these elements offers a distinctive opportunity to probe the limits of the periodic table and explore the "island of stability", characterized by magic numbers $Z = 120, 126$ and $N = 184$ [1–6]. Numerous theoretical and experimental studies have offered valuable insights into the synthesis of SHN via heavy-ion-induced reactions. These studies revealed several factors that influence the dynamics of these reactions within the low-energy domain [7–15]. Firstly, for the synthesis of SHN, the interacting nuclei need to overcome the repulsive Coulomb barrier to subsequently create a compound nucleus through the exchange of nucleons and energy. The characteristics of this Coulomb barrier, i.e the barrier height V_B and barrier position R_B , play a significant role, as they can hinder the formation of the new entity

[16–19]. Studies around the Coulomb barrier of such interactions suggest that numerous parameters like mass, charge, energy, deformations, orientations, and angular momentum of the interacting nuclei can significantly influence the barrier height V_B and barrier position R_B of the Coulomb barrier [20–24]. Among these degrees of freedom, deformations of the interacting nuclei have been found to play a critical role in influencing both the barrier characteristics and the production of heavy and superheavy nuclei. Numerous investigations have been conducted in the literature studying the influence of quadrupole (β_2) deformations of interacting nuclei, on the barrier characteristics and the capture cross-sections σ_{cap} [25–29]. The promising results of these investigations encourage us to study in depth the influence of these higher-order deformations to explore adequate assessment of the reaction dynamics.

Recent studies have examined the effects of higher-order deformations on the synthesis of SHN, specifically focusing on octupole (β_3) and hexadecapole (β_4) deform-

Received 15 August 2025; Accepted 6 November 2025

[†] E-mail: dpathania1630@gmail.com

[‡] E-mail: hsharma.nph@gmail.com

[§] E-mail: msharma@thapar.edu

©2026 Chinese Physical Society and the Institute of High Energy Physics of the Chinese Academy of Sciences and the Institute of Modern Physics of the Chinese Academy of Sciences and IOP Publishing Ltd. All rights, including for text and data mining, AI training, and similar technologies, are reserved.

ations [25, 30–38]. Till date a very few studies have analyzed and discussed the influence of hexacontatetrapole (β_6) and octacontatetrapole (β_8) deformations on the dynamics of heavy-ion induced reactions. So there remains a lack of explicit analysis and comprehension concerning the influence of β_6 and β_8 deformations. Furthermore, while the experimental evidence for the presence of β_6 in proton and alpha scattering from ^{238}U [39, 40] and ^{154}Sm [41] and on fusion reaction dynamics [37, 38, 42, 43], intrigues interest in the characteristics of β_6 , similar insights regarding the β_8 deformation cannot be made due to the absence of experimental data. In view of this, it is of interest to investigate the influence and effect of the β_6 deformation on the synthesis of SHN via heavy-ion induced fusion reactions.

In view of the deformations of the interacting nuclei, the elongated and compact configurations, determined by the extremes of the interaction barrier height (V_B) and the barrier position (R_B), play a critical role in influencing the reaction dynamics [17, 29, 36]. While the configuration with the maximum V_B and minimal R_B is termed a compact configuration, the configuration with the minimal V_B and the maximal R_B is referred to as the elongated configuration. The influence of these configurations has been discussed and established in [17, 36, 44–47]. These configurations are significantly influenced by the incorporation of higher-order deformations. Therefore, in the present work, the relevance of the β_6 deformation and associated orientations will be analyzed in reference to the barrier characteristics and capture cross-sections in the context of reactions leading to the synthesis of SHN.

For our analysis, we have considered the P-T combinations $^{48}\text{Ca}+^{248}\text{Cm}$, $^{48}\text{Ca}+^{244}\text{Pu}$, $^{48}\text{Ca}+^{238}\text{U}$, $^{36}\text{S}+^{238}\text{U}$ and $^{48}\text{Ti}+^{238}\text{U}$ leading to the formation of SHN ^{296}Lv , ^{292}Fl , ^{286}Cn , ^{274}Hs and ^{286}Fl respectively. The barrier characteristics of the modified nuclear shape due to the collective influence of the magnitude and sign (\pm) of the deformations (up to β_6) of the actinide target nuclei and their corresponding orientations are then used to determine the capture cross-sections (σ_{cap}) for the considered P-T combinations using the ℓ -summed Wong formula [48, 49]. The static deformation parameters $\beta_2, \beta_4, \beta_6$ are taken from the Data Table of Möller et al. [50]. The capture cross-sections (σ_{cap}) are calculated for center of mass energies ($E_{c.m.}$) spread across the Coulomb barrier, and are subsequently compared with the experimental data available as referenced in [51]. Furthermore, the influence of magnitude and signs of $\beta_2^\pm, \beta_4^\pm, \beta_6^\pm$ deformation is studied by considering the P-T combination $^{48}\text{Ca}+^{246}\text{Es}$ having significant magnitude of all deformations at energy range of $E_{c.m.} = 180\text{--}220$ MeV spanning the Coulomb barrier. Thus, the present work provides a thorough analysis of the modified barrier characteristics and reaction dynamics incorporating the β_2^\pm, β_4^\pm , and β_6^\pm deformations. These findings advance our comprehension further in the direc-

tion of understanding and unraveling the complexity of the dynamics associated with heavy-ion-induced reactions leading to the formation of SHN.

This manuscript is structured as follows: Section II provides a theoretical framework. Section III presents and discusses the results, emphasizing the role of the magnitude and signs (\pm) of hexacontatetrapole deformations (β_6) on the nuclear shape of deformed nuclei, the barrier characteristics, and the fusion reaction dynamics of actinides. Finally, Section IV presents a summary of the work done.

II. METHODOLOGY

A. Shape determination of the deformed nucleus

The shape of the deformed nuclei can be expressed by the radial vector $R_i(\alpha_i)$ equation in terms of the spherical harmonics $Y_{\lambda i}^{(0)}(\alpha_i)$ and the magnitude of the deformation $\beta_{\lambda i}$ [43, 50, 52, 53], as

$$\begin{aligned} R_i(\alpha_i) &= R_{0i} \left[1 + \sum_{\lambda=2,3,4,6} \beta_{\lambda i} Y_{\lambda i}^{(0)}(\alpha_i) \right] \\ &= R_{0i} \left[1 + \sum_{\lambda=2,3,4,6} \beta_{\lambda i} \sqrt{\frac{2\lambda+1}{4\pi}} P_{\lambda}(\cos \alpha_i) \right], \quad (1) \end{aligned}$$

Here, the $i = 1, 2$ denotes the projectile and target of the interacting systems, respectively. The term R_{0i} signifies the radius of the spherical nuclei, defined by the equation $R_{0i} = 1.28A_i^{1/3} - 0.76 + 0.8A_i^{-1/3}$, measured in femtometers (fm) [54]. The variable λ indicates the degree of deformation present in the nuclei, with values $\lambda = 2, 3, 4, 6$ corresponding to quadrupole, octupole, hexadecapole, and hexacontatetrapole deformations, respectively. The static deformation parameter $\beta_{\lambda i}$ is taken from the Data Table of Möller et al. [50]. The function $P_{\lambda}(\cos \alpha_i)$ represents the Legendre polynomial.

B. Total interaction potential

The colliding nuclei interact through an interaction potential (V_T), which comprises the sum of the attractive nuclear potential (V_N), repulsive Coulomb potential (V_C), and centrifugal potential (V_{ℓ}). The total interaction potential V_T is quantitatively expressed as follows:

$$\begin{aligned} V_T(R_i, A_i, \beta_{\lambda i}, \theta_i) &= V_N(R_i, A_i, \beta_{\lambda i}, \theta_i) \\ &+ V_C(R_i, A_i, \beta_{\lambda i}, \theta_i) + V_{\ell}(R_i, A_i, \beta_{\lambda i}, \theta_i), \quad (2) \end{aligned}$$

In Eq.2, the attractive nuclear potential is represented by V_N , among the two interacting nuclei. It is calculated using a generalized theorem for proximity forces, given by Blocki and collaborators in 1977, called Prox77 [54]. The

nuclear potential $V_N(R, A_i, \beta_{Ai}, \theta_i)$ reads as[54–58]

$$V_N(R, A_i, \beta_{Ai}, \theta_i) = 4\pi\bar{R}\gamma b\Phi(s_0), \quad (3)$$

Here, b' is the surface diffuseness parameter and has a constant value of 0.99 fm.

The mean curvature radius (\bar{R}) is evaluated in terms of radius vector of curvatures R_{i1} and R_{i2} for projectile and target nuclei respectively, as follows:

$$\frac{1}{\bar{R}^2} = \frac{1}{R_{11}R_{12}} + \frac{1}{R_{21}R_{22}} + \frac{1}{R_{11}R_{22}} + \frac{1}{R_{21}R_{12}}. \quad (4)$$

The principal radii of curvature (R_{i1} and R_{i2}) for deformed-deformed or spherical-deformed cases is given [56] as

$$R_{i1}(\alpha_i) = \frac{[R_i^2(\alpha_i) + R_i'^2(\alpha_i)]^{3/2}}{R_i^2(\alpha_i) + 2R_i'^2(\alpha_i) - R_i(\alpha_i)R_i''(\alpha_i)}, \quad (5)$$

$$R_{i2}(\alpha_i) = \frac{R_i(\alpha_i) \sin \alpha_i}{\cos(\pi/2 - \alpha_i - \delta_i)} \quad (i = 1, 2). \quad (6)$$

For the spherical projectiles, this Eq. 5 is simplified as $R_{i1}(\alpha_i) = R_{i2}(\alpha_i) = R_i(\alpha_i)$. In Eq.(3) the surface energy constant (γ) is expressed in terms of the asymmetry of nucleons as,

$$\gamma = 0.9517 \left[1 - 1.7826 \left(\frac{N-Z}{A} \right)^2 \right] \text{ MeVfm}^{-2}, \quad (7)$$

The term $4\pi\bar{R}\gamma b$ in Eq.(3) takes care of the shape and geometry of the colliding nuclei. While the universal function dependent on the shortest distance parameter (s_0) between the colliding nuclei along the collision axis is given as [55, 56],

$$\Phi(s_0) = \begin{cases} -\frac{1}{2}(s_0 - 2.54)^2 - 0.0852(s_0 - 2.54)^3, & s_0 \leq 1.2511 \text{ fm} \\ -3.437 \exp\left(-\frac{s_0}{0.75}\right), & s_0 > 1.2511 \text{ fm}. \end{cases} \quad (8)$$

Here, the s_0 is the shortest distance between the two interacting nuclei [56], which is defined as

$$s_0 = R - X_1 - X_2, \quad (9)$$

Where 'R' represents the distance between the interacting nuclei and X_1, X_2 are the projections of P-T nuclei w.r.t.

the colliding axis. These projections are determined as

$$\begin{aligned} X_1 &= R_1(\alpha_1) \cos(\theta_1 - \alpha_1); \\ X_2 &= R_2(\alpha_2) \cos(180 + \theta_2 - \alpha_2) \end{aligned} \quad (10)$$

With the minimization conditions on s_0 we get,

$$\begin{aligned} \tan(\theta_1 - \alpha_1) &= \tan(\delta_1) = -\frac{R_1'(\alpha_1)}{R_1(\alpha_1)}, \\ \tan(180 + \theta_2 - \alpha_2) &= \tan(\delta_2) = -\frac{R_2'(\alpha_2)}{R_2(\alpha_2)}. \end{aligned} \quad (11)$$

The repulsive Coulomb potential (V_C) in Eq.(2) is defined for deformed-deformed colliding nuclei as follows[59, 60]:

$$\begin{aligned} V_C(R) &= \frac{Z_1 Z_2 e^2}{R} + Z_1 Z_2 e^2 \sum_{\lambda=2,3,4,6}^{i=1,2} \left(\frac{R_i^\lambda(\alpha_i)}{R^{\lambda+1}} \right) \beta_\lambda Y_\lambda^{(0)}(\theta_i) \\ &\times \left[\frac{3}{2\lambda+1} + \left(\frac{12}{7(2\lambda+1)} \right) \beta_\lambda Y_\lambda^{(0)}(\theta_i) \right]. \end{aligned} \quad (12)$$

The centrifugal potential (V_ℓ), mentioned in Eq. 12 is the rotational kinetic energy. This potential is dependent on the angular momentum ℓ and is formulated as follows [61, 62]:

$$V_\ell(R, A_i, \beta_{Ai}, \theta_i) = \frac{\hbar^2 \ell(\ell+1)}{2I}; \quad I = \mu R^2. \quad (13)$$

The equations (2) - (13) that define the total interaction potential provide significant insights into the characteristics of the interacting nuclei. This encompasses barrier characteristics, including the barrier height V_B , the barrier position R_B , and the barrier curvature $\hbar\omega_B$. These parameters are affected by the degrees of freedom related to deformation and orientation, as indicated in the radius vector presented in Eq.(1). As a result, these parameters play a crucial role in finding the capture cross-sections, which is calculated by using the ℓ -Wong formula [48, 49] for different combinations of the interacting P-T, briefed in the next section.

C. Capture cross-sections

The capture cross-section for deformed and oriented nuclei, interacting at the center of mass energies ($E_{c.m.}$), is evaluated using the Wong formula [59, 63], which reads as

$$\sigma_{cap} = \frac{R_B^2 \hbar\omega_B}{2E_{c.m.}} \ln \left[1 + \exp \left(\frac{2\pi}{\hbar\omega_B} (E_{c.m.} - V_B) \right) \right], \quad (14)$$

which further, transforms to the extended ℓ -summed

Wong Model [48, 49]. This model incorporates the summation of the cross-section associated with each ℓ -partial wave, which can be mathematically represented as follows:

$$\sigma_{cap}(E_{c.m.}, \theta_i) = \sum_{\ell=0}^{\ell_{max}} \sigma_{\ell} = \frac{\pi}{k^2} \sum_{\ell=0}^{\ell_{max}} (2\ell+1) P_{\ell}, \quad (15)$$

where $k = \sqrt{\frac{2\mu E_{c.m.}}{\hbar^2}}$ and μ represents the reduced mass. The sharp cut-off approximation [55, 64] is employed to determine the maximum angular momentum, denoted as ℓ_{max} . Here, the barrier penetration or tunneling probability P_{ℓ} for each angular momentum (ℓ) is derived using the Hill-Wheeler approximation [65].

$$P_{\ell}^{HW}(E_{c.m.}) = \left[1 + \exp\left(\frac{2\pi[V_B^{\ell}(E_{c.m.}) - E_{c.m.}]}{\hbar\omega_B^{\ell}(E_{c.m.})}\right) \right]^{-1}, \quad (16)$$

In this Eq. the $V_B^{\ell}(E_{c.m.})$, $R_B^{\ell}(E_{c.m.})$ and $\hbar\omega_B^{\ell}(E_{c.m.})$ are obtained from the total interaction potential between the two interacting nuclei determined in Eq. 2.

In addition, the integrated or average capture cross-sections are obtained by integrating over the range of orientations θ_i of the deformed nuclei having $\beta_2, \beta_4, \beta_6$ deformations [47], which is represented as

$$\sigma_{int}(E_{c.m.}) = \int_{\theta_1=0}^{\pi/2} \int_{\theta_2=0}^{\pi/2} \sigma(E_{c.m.}, \theta_i) \sin\theta_1 \sin\theta_2 d\theta_1 d\theta_2. \quad (17)$$

III. RESULT AND DISCUSSION

In the present work, we aim to explore the influence of the modified nuclear shape due to the incorporation of hexacontatetrapole deformation (β_6) along with (β_2), (β_4) deformed target nuclei. This study systematically investigates the collective influence of magnitude and sign (\pm) of these higher-order deformations (up to β_6) on barrier characteristics of heavy-ion induced fusion reactions. Further, the elongated and compact configurations obtained from these modified barrier characteristics corresponding to β_4 and β_6 deformations are used to calculate the capture cross-sections (σ_{cap}) which are compared with available experimental data, for center of mass energies $E_{c.m.}$ spread across the Coulomb barrier. The analysis takes into account both spherical+deformed and deformed+deformed P-T combinations. This comprehensive study offers new insights into the influence of higher-order deformations up to the order of hexacontatetrapole deformation (β_6) on the fusion reaction dynamics. The findings of this work are presented and discussed in the following sections.

A. Nuclear Shape of hexacontatetrapole (β_6) deformed nuclei

The nuclear shape usually shows deviations from perfect spherical symmetry. These deviations arise from dipole moments linked to the neutron-to-proton ratio within the nuclei, leading to a deformed nuclear shape. These nuclear deformations (β_{λ}) associated with the multipole order i.e. $\lambda=2,3,4,6$ provides quadrupole, octupole, hexadecapole and hexacontatetrapole deformed shapes of nuclei respectively. The influence of these higher-order deformations is included in the nuclear shape via the radial vector as defined in Eq. (1). To visualize the influence of β_6 deformation on nuclear shape, we considered ^{246}Es nuclei having significant magnitude of β_2 taken from the data table of Möller et al. [50], while deformations $\beta_4 = \pm 0.05$ and $\beta_6 = \pm 0.1$ are assumed to analyze the significant effect of β_6 , shown in Fig. (1). The figure illustrates the evolution of the nuclear shape of ^{246}Es by incorporating different orders of deformations. One can see the evolution of prolate-deformed nuclei with the incorporation of β_4^+ and β_6^+ deformations associated with the nuclei. It is known that the incorporation of β_4^+ with β_2^+ leads to elongation, whereas the inclusion of β_4^- with β_2^+ leads to contraction of the prolate deformed nuclei. While Fig. 1(a) illustrates the modification in nuclear shape after the inclusion of β_6^+ in $\beta_2^+\beta_4^+$ deformed nuclei, figure 1(b) represents similar modifications in shape of $\beta_2^+\beta_4^-$ deformed nuclei due to the incorporation of β_6^+ . It can be seen from the figures that the incorporation of β_6^+ deformation introduces complexity to both the elongated shape of $\beta_2^+\beta_4^+$ deformed nuclei and the compressed shape of $\beta_2^+\beta_4^-$ deformed nuclei. Specifically, the presence of β_6^+ in both β_4^+ , leads to further elongation of nuclear shape along its poles, and slight compression along the belly region of the nuclei. This elongation due to β_6^+ is more pronounced in the $\beta_2^+\beta_4^+$ case than the $\beta_2^+\beta_4^-$ deformed nuclei. On the other hand, β_6^- leads to compression on the poles and elongation along the belly, when incorporated in both β_4^+ and β_4^- . This flatness is more prominent at poles for $\beta_2^+\beta_4^-$ deformed nuclei than $\beta_2^+\beta_4^+$, as shown in Fig1.

In other words, the incorporation of β_6^+ leads to elongation at the poles region and compression at the belly region, whereas β_6^- leads to the elongation at the belly region and compression at poles. In addition to the sign (\pm) of the hexacontatetrapole deformation, the extent of the elongation and compression in the deformed nuclear shape is also influenced by the magnitudes of the deformation associated with the nuclei. The above observations highlight the sensitivity of nuclear shapes to the magnitude and signs of higher-order deformations, specifically β_6 in conjunction with β_2 and β_4 deformations. These modifications due to the collective influence of $\beta_2\beta_4\beta_6$ deformations provide significant modifications on the nuclear barrier characteristics that govern the heavy-ion

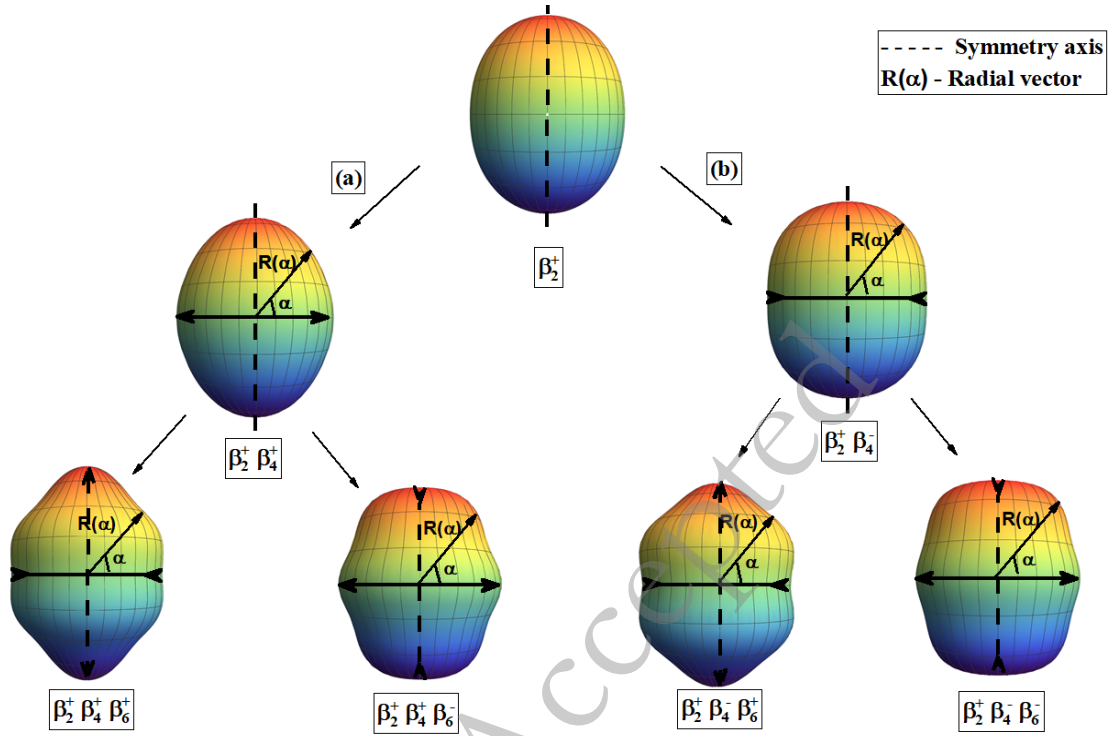


Fig. 1. (color online) Schematic diagram of shape evolution of the nucleus ^{246}Es incorporating the quadrupole (β_2), hexadecapole (β_4^\pm) and hexacontatetrapole (β_6^\pm); with $\beta_2=0.248$, considering $\beta_4 = \pm 0.05$ and $\beta_6 = \pm 0.1$

fusion dynamics. The upcoming section discusses the effect of these deformed nuclear shapes on the barrier characteristics relative to the angle of orientations of the deformed nuclei with respect to the collision axis.

B. Analysis of barrier characteristics of the hexadecapole (β_4) and hexacontatetrapole (β_6) deformed actinide targets

In the previous section, we discussed the influence of the magnitude and sign of the β_6^\pm on the shape of the nuclei along with the β_2^\pm and β_4^\pm deformations. This current section aims to broaden the analysis by investigating the comprehensive effect of the modified shape of β_4^\pm and β_6^\pm deformed nuclei on the barrier characteristics i.e. barrier height (V_B) and barrier position (R_B) of the interacting nuclei. The objective of this analysis is to determine how the incorporation of β_4^\pm and β_6^\pm deformations modifies the barrier characteristics when compared to a prolate deformed (β_2^\pm) case. For this analysis, we investigated the barrier characteristics for the ^{48}Ca -induced reactions with deformed actinide nuclei having non-zero values of β_2 , β_4 , and β_6 deformations. The variation in V_B and R_B with respect to target orientation (θ_2) ranging from 0° to 180° for different combinations of β_2 , β_4 , and β_6 deformations are illustrated in Fig.2 and Fig.3 respectively. From these figures, one can see that here the cases are divided into two panels with panel (I) representing the barrier characteristics of $\beta_2^\pm \beta_4^\pm \beta_6^\pm$ deformed nuclei while panel (II)

represents the barrier characteristics of $\beta_2^\pm \beta_4^\mp \beta_6^\pm$ deformed nuclei. Each panel of the analyzed actinide nuclei is classified into three distinct groups based on the values of β_4 and β_6 deformations. In particular, Fig.2(a, b, g and h) illustrates the scenarios where the magnitude of β_4 is greater than β_6 , while Fig.2(c, d, i and j) depicts the cases where magnitude of β_4 is approximately equal to magnitude of β_6 deformation. Additionally, Fig.2(e, f, k and l) showcases the instances where the magnitude of β_6 deformation exceeds the magnitude of β_4 deformation. To conduct a thorough analysis of both the sign and magnitude of the associated β_6 deformation, both positive and negative β_6 deformations of equal magnitude are considered.

From these figures, one can observe that the introduction of β_4^\pm in quadrupole deformed nuclei leads to a lowering of the barrier height V_B . Conversely, the incorporation of β_4^\mp in β_2 deformed nuclei leads to an increase in V_B . The relative variation in the V_B is influenced by the magnitudes of the β_2 and β_4 deformation parameters. Along with the barrier characteristics, a noticeable change in the orientation angle of the compact and elongated configurations has also been observed [36]. Further, the incorporation of β_6^\pm in conjunction with β_2 and β_4 deformation modifies the shape of the nuclei at both the pole and belly positions, leading to variation in the barrier characteristics V_B and R_B . For instance, incorporation of β_6^\pm to $\beta_2^\pm \beta_4^\pm$ deformed nuclei lowers the barrier height V_B specifically at target orientation $\theta_2=0^\circ$ or 180° . Mean-

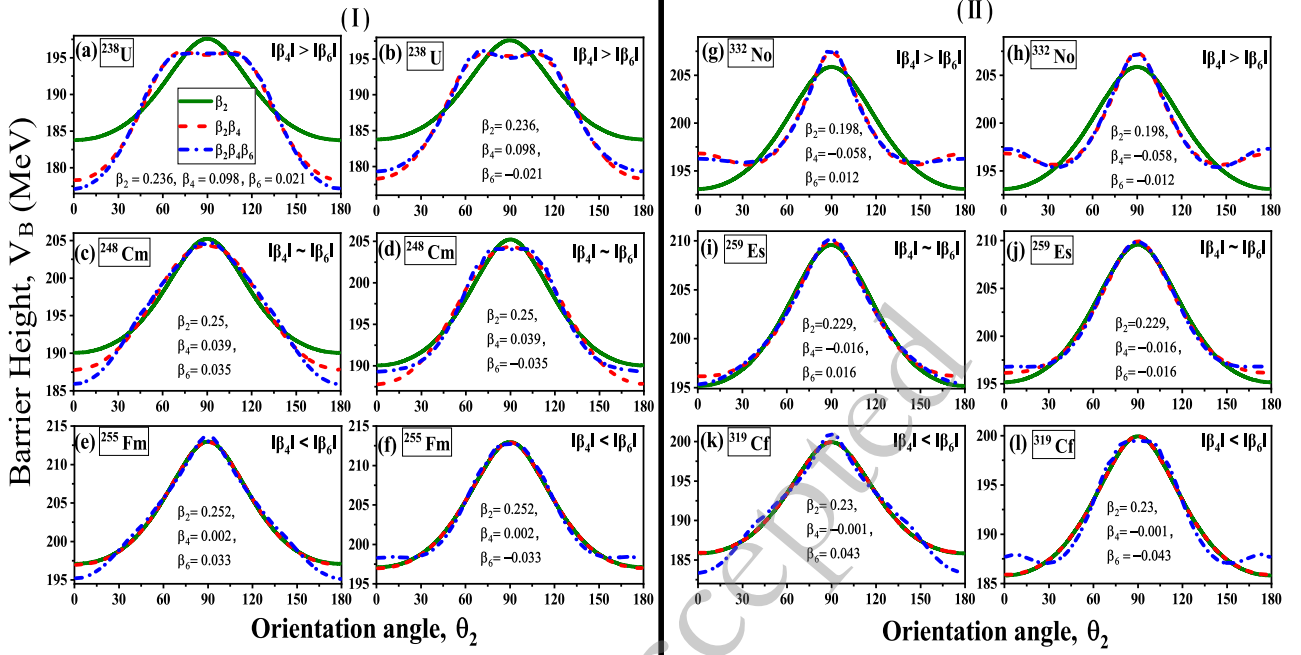


Fig. 2. (color online) A schematic representation illustrating the changes in barrier height (V_B) in relation to the orientation angle (θ_2) of deformed actinide nuclei. Panel (I) features nuclei with configurations $\beta_2^+ \beta_4^+ \beta_6^+$, while Panel (II) showcases $\beta_2^+ \beta_4^- \beta_6^+$ deformed nuclei.

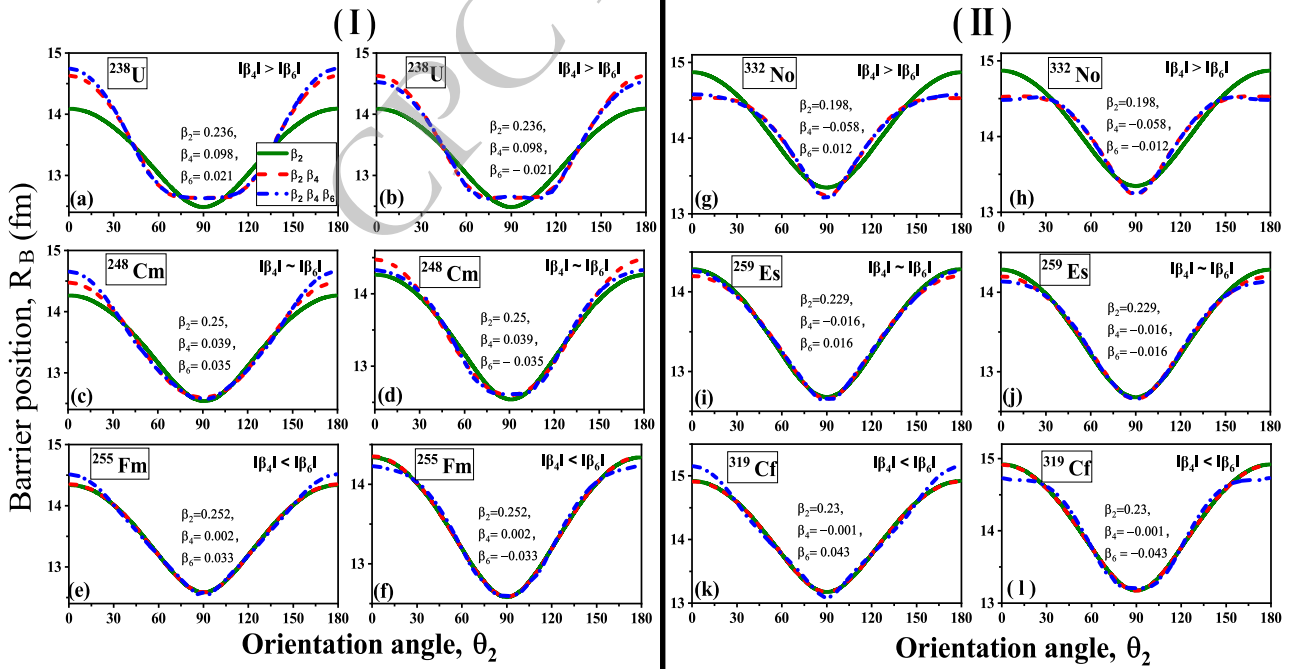


Fig. 3. (color online) A schematic representation illustrating the changes in barrier position (R_B) in relation to the orientation angle (θ_2) of deformed actinide nuclei. Panel (I) features nuclei with configurations $\beta_2^+ \beta_4^+ \beta_6^+$, while Panel (II) showcases $\beta_2^+ \beta_4^- \beta_6^+$ deformed nuclei.

while, β_6^- increases the barrier height due to compression of the shape of the nuclei around the poles at $\theta_2=0^\circ$ or 180° . The impact of β_6^- deformations is more pronounced for the orientations in the range of 0° - 40° for all the

cases. However, as θ_2 surpasses this range, there is a slight change in the V_B corresponding to $\beta_2 \beta_4 \beta_6^-$ deformed nuclei as compared to $\beta_2 \beta_4$ deformed nuclei. Conversely, an interesting variation can be observed at target

orientation $\theta_2 = 90^\circ$. At this orientation, the barrier height V_B increases for the β_6^+ cases while a decrease in V_B can be observed for the β_6^- cases relative to β_4 . This variation, as discussed in the previous section, is linked to compression and elongation of the nuclear shape at the belly of the nuclei due to the incorporation of β_6^+ and β_6^- deformations, respectively. It is important to note that the variation of V_B is not very significant at 90° for all the cases. Additionally, in scenarios where the value of β_4 is greater than β_6 and β_4 is approximately equal to β_6 , the changes in barrier characteristics resulting from the inclusion of β_6 correspond to the deformation trend of β_4 . Conversely, in instances where β_4 is less than β_6 , as illustrated in Fig.2(e,f,k,l), the substantial impact of β_6 is evident due to its significantly larger magnitude relative to β_4 . In a similar manner, an inverse variation with respect to V_B is observed in the analysis of barrier position R_B for all the considered reactions. The variation of R_B for the considered reactions w.r.t orientation angle (θ_2) are illustrated in Fig.3.

Along with the variation in the barrier characteristics V_B and R_B , a significant shift in the optimum orientation can also be observed with the incorporation of β_6 . These modified optimum orientations of the compact or elongated configuration of the β_6 deformed nuclei can impose a significant influence on the overall dynamics of the nuclear interaction. These modified compact or elongated configurations are characterized by the maximal and

minimum values of barrier height (V_B) and barrier position (R_B). While the elongated configuration corresponds to the configuration with the minimum V_B and maximum R_B , whereas the compact configuration is the configuration associated with the maximum V_B and minimum R_B . The analysis of the barrier height corresponding to $\beta_2, \beta_4, \beta_6$ in relation to the orientation angle (θ_2) is shown in Fig.2. The figure clearly demonstrates that the variation in the barrier height V_B due to incorporation of β_6 deformation in comparison to the β_4 deformation is significantly more pronounced in the orientation range $\theta_2=0^\circ$ to 40° than those at $\theta_2=70^\circ$ to 90° . The orientation range $\theta_2=0^\circ$ to 40° represents the region with the minimum barrier height or the elongated configuration, while the orientation range $\theta_2=70^\circ$ to 90° represents the region with the maximum barrier height or the compact configuration for the $\beta_2\beta_4\beta_6$ deformation combinations, respectively. Based on these results, additional emphasis will be placed on evaluating the impact of β_6 on the barrier characteristics at orientation angles ranging from 0° to 40° .

Till now, we have established that the incorporation of β_6 deformation along with β_2 and β_4 provides noticeable alterations in the barrier characteristics for orientation angles ranging from 0° to 40° . Further to explore the influence of the magnitude of β_6 we studied the variation in the V_B for the above-mentioned range of orientation angle by varying the magnitude of β_6 deformation from -0.05 to 0.05 as demonstrated in Fig.4. For the analysis,

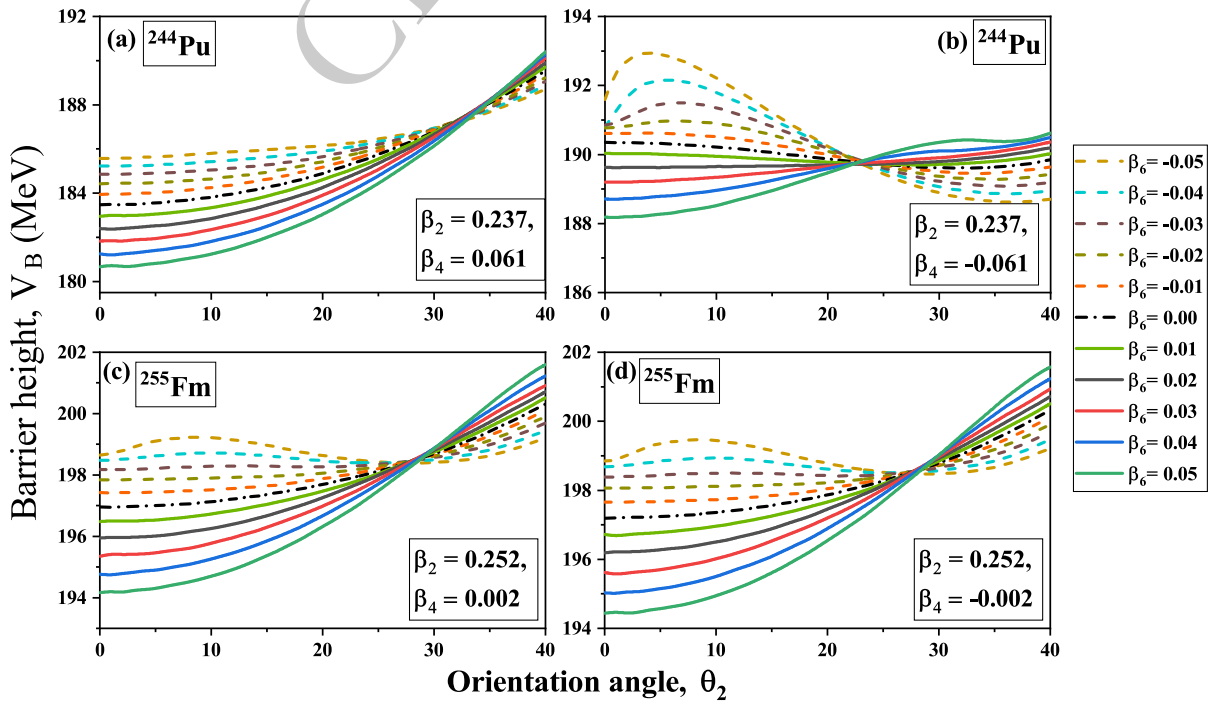


Fig. 4. (color online) Schematic diagram showing the variation of barrier height with respect to the orientation angle of the target varying from 0° – 40° , under different values of β_6 ranging from -0.05 to $+0.05$ for nucleus with significant β_4^\pm (^{244}Pu) and nucleus with small magnitude of β_4^\pm (^{255}Fm).

we consider the actinide nuclei having a significant magnitude of β_4 deformation as compared to the magnitude of β_6 (e.g. ^{244}Pu), and the nuclei with a smaller magnitude of β_4 deformation as compared to the magnitude of β_6 (e.g. ^{255}Fm). Note that the study assumes both positive and negative signs for the magnitude of β_4 of the same nuclei. From Fig.4, it can be observed that an increase in the magnitude of β_6^+ introduces much significant elongation to the nucleus along its poles, leading to a decrease in barrier height with respect to β_4^+ at $\theta_2 = 0^\circ$ or 180° . Conversely, an increase in the magnitude of β_6^- induces an increase in the barrier height due to an enhanced compression effect along the poles. As we move towards the target orientation $\theta_2 = 30^\circ$, variations in barrier height V_B can be observed for both β_6^+ and β_6^- cases. It is observed that increasing the positive value of β_6^+ leads to a high V_B while increasing the negative value of β_6^- results in a lower V_B at 30° or above, compared to $\beta_2\beta_4$ deformed nuclei. These variations are due to shape modifications caused by the incorporation of β_6^\pm . In Fig.4(a), ^{244}Pu have a significant magnitude of β_4^+ , the elongated shape always appears at orientation angle $\theta_2 = 0^\circ$, regardless of the magnitude of β_6^\pm . However, in Fig.4(b), a large negative β_4^- induces the compression in the nuclear shape, and the orientation angle for the elongated configuration shifts to around $\theta_2 = 30^\circ$. When β_6^+ is added, it reduces this compression and brings back elongation at the poles $\theta_2 = 0^\circ$ as its values increase. On the other hand, β_6^- makes the compression at the poles even stronger, reinforcing the minimum barrier height around $\theta_2 = 30^\circ$.

On the other hand, for a smaller magnitude of β_4^\pm , the shape of nuclei is majorly influenced by the magnitude and sign of β_6 deformation. For instance, for both the cases of β_6 , the elongated configuration is observed at $\theta_2 = 0^\circ$ or 180° as illustrated in Fig.4(c,d). However, this ori-

entation angle for elongation configuration gets shifted towards $\theta_2 \approx 30^\circ$ for the higher magnitude of β_6^- . This analysis indicates that the magnitude and sign of the β_6 deformation have a significant influence on the barrier height V_B at the elongated configuration and also can shift the elongated configuration from 0° to around 30° , in conjunction with the influence of $\beta_2\beta_4^\pm$ deformations.

In order to conduct an in-depth analysis of the variation in barrier height V_B at the elongated configuration, we examined different sign combinations of quadrupole (β_2), hexadecapole (β_4), and hexacontatetrapole (β_6) deformations. This investigation focuses on several actinide nuclei to provide a comprehensive analysis of magnitudes and signs of deformations. Considered nuclei are examined by comparing the magnitudes of β_4 and β_6 deformation, categorized into three sets: (a) $\beta_4 > \beta_6$, (b) $\beta_4 \approx \beta_6$, and (c) $\beta_4 < \beta_6$. These three sets are analyzed for the deformation combinations specifically $\beta_2^+\beta_4^+\beta_6^+$, $\beta_2^+\beta_4^+\beta_6^-$, $\beta_2^+\beta_4^-\beta_6^+$, and $\beta_2^+\beta_4^-\beta_6^-$, as presented in Fig.5. The deformations of the considered nuclei are taken from the data table of Möller et al. [50], and the magnitudes of β_4 and β_6 are considered with both positive and negative signs for the analysis. The analysis of the figure reveals that for the combinations $\beta_2^+\beta_4^+\beta_6^+$ and $\beta_2^+\beta_4^-\beta_6^-$, the incorporation of β_6^+ results in a reduction of the barrier height (V_B), whereas incorporation of β_6^- counteracts the influence of β_4^+ , thus resulting in an increase in V_B when added to the deformed nuclei of $\beta_2^+\beta_4^+$. This result is consistent across all sets of magnitudes of β_4 and β_6 , as depicted in Fig.5. While the same trend of variation in barrier height is obtained for β_6^+ and β_6^- when incorporated in the $\beta_2^+\beta_4^-$ deformed nuclei. These effects of β_6^+ and β_6^- are consistent when incorporated with $\beta_2^+\beta_4^-$ deformation combination but specific to scenarios where $\beta_4 \approx \beta_6$ and $\beta_4 < \beta_6$, where the magnitude of β_4 is not much significant-

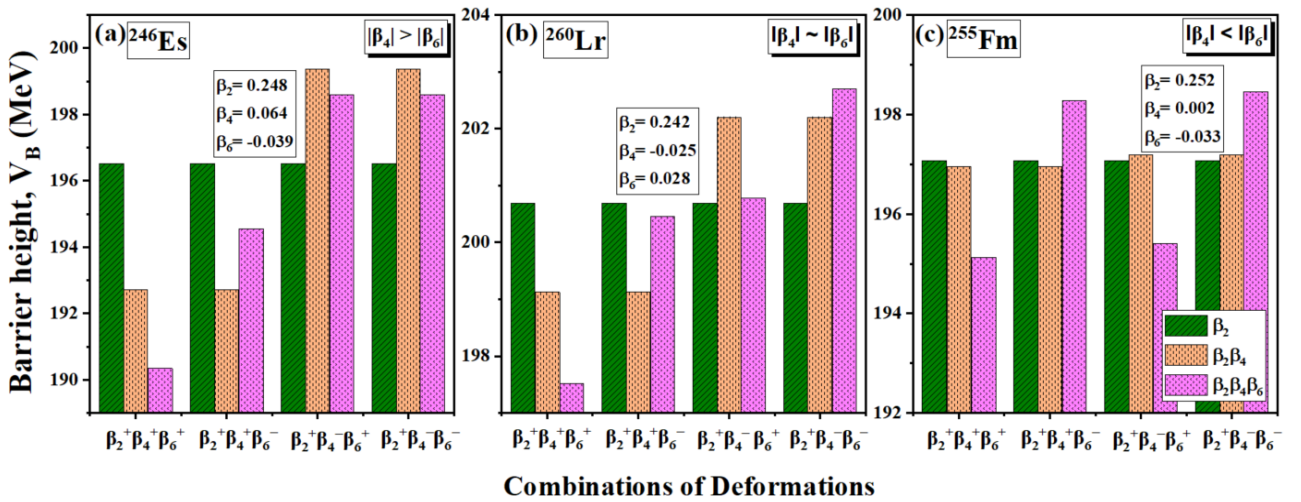


Fig. 5. (color online) Schematic diagram of comparison of the barrier heights of nuclei at elongated configuration corresponding to different combinations of deformations $\beta_2^+\beta_4^+\beta_6^+$, $\beta_2^+\beta_4^+\beta_6^-$, $\beta_2^+\beta_4^-\beta_6^+$, and $\beta_2^+\beta_4^-\beta_6^-$ for the considered nuclei having variation of magnitudes such as (a) $\beta_4 > \beta_6$, (b) $\beta_4 \approx \beta_6$, (c) $\beta_4 < \beta_6$.

ant, as illustrated in Fig.5(b,c). However, besides this, a minor deviation in this trend occurs when $\beta_4 > \beta_6$ case is considered, as shown in Fig.5(a). Contrary to expectations, the addition of β_6^+ and β_6^- does not yield the anticipated decrease and increase in V_B when combined with β_4^- . This seems to indicate that the predominance of β_4 over β_6 induces a structural modification. Further explicit analysis is necessary to quantify the interactions among these deformation parameters in the case of $\beta_4 > \beta_6$ and to assess their collective impact on the barrier characteristics, specifically at the elongation configuration.

To further examine the influence of the β_6^\pm deformation in the presence of a substantial β_4^- deformation, we conducted an analysis of the variations in V_B at elongated configurations for several nuclei illustrated in Fig.6. In this context, we refer to Fig.4(b), which demonstrates that the magnitude of β_4^- is considerable to the magnitude of the β_6^\pm where the presence of β_4^- deformation contributes to the overall shape of the nuclei. As previously mentioned, an increase in the magnitude of β_6^+ is associated with a decrease in V_B , leading to elongation at an angle of 0° . However, for lower magnitudes of β_6^\pm , both compression and elongation effects arise due to β_4^- and β_6^\pm , respectively, creating a balance in the shape that results in a higher V_B than that produced solely by β_4^- . On the other hand, the β_6^- deformation intensifies the compression at poles but continues the elongation near $\theta_2 \approx 30^\circ$, resulting in a decrease in V_B as its magnitude increases. The relevant evidence for this behavior in the

nuclei is depicted in Fig.6(c,d). Meanwhile, as the magnitudes of both β_6^+ and β_6^- deformations rise, the values of V_B become comparable. This behavior is illustrated in Fig.6(a,b), which shows the comparable and lower values of V_B for β_6^\pm in relation to β_4^- . Nevertheless, the relative change in V_B for β_6^\pm compared to β_4^- is not significant.

The above discussion explored the role of hexacontatetrapole deformations in heavy-ion induced reactions for a spherical projectile (^{48}Ca) with β_6 deformed target actinide nuclei and provided significant results. Furthermore, we intend to analyze the influence of the projectile orientation (θ_1) on barrier characteristics for deformed-deformed P-T combinations. Therefore, the variation of the barrier height V_B with respect to the orientation angle of both the deformed target and projectile nuclei is systematically analyzed through the color-mapped contour plots for the reactions having minimum and significant magnitude of projectile deformation, respectively, in Fig.7. For the reaction ^{48}Ti ($\beta_2 = 0.011$) + ^{238}U ($\beta_2 = 0.236$, $\beta_4 = 0.098$, $\beta_6 = -0.021$), as the magnitude of β_2 deformation of projectile is smaller, therefore the barrier height V_B is less sensitive to the projectile orientation and there is no significant change in the orientation angles for the compact and elongated configurations, as shown in Fig.7(a). While the compact configuration with the highest barrier height occurs at $\theta_1 = 97^\circ, \theta_2 = 110^\circ$, the elongated configuration with the lowest barrier is observed at $\theta_1 = 1^\circ, \theta_2 = 0^\circ$. These configurations are dependent on the target orientation i.e., a change in the pro-

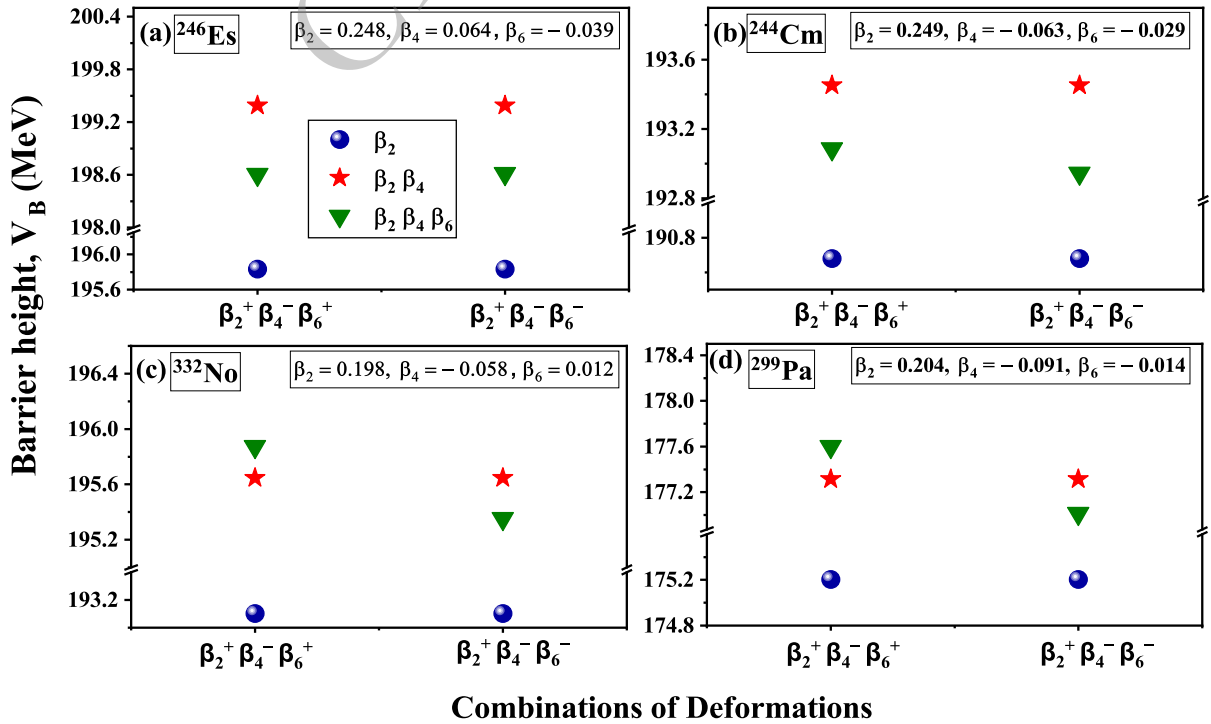


Fig. 6. (color online) Schematic diagram of comparison of the barrier heights of different actinides with ^{48}Ca projectile at the elongated configuration for the $\beta_2^+\beta_4^-\beta_6^+$, and $\beta_2^+\beta_4^-\beta_6^-$ combination of deformations in the case of $\beta_4 > \beta_6$.

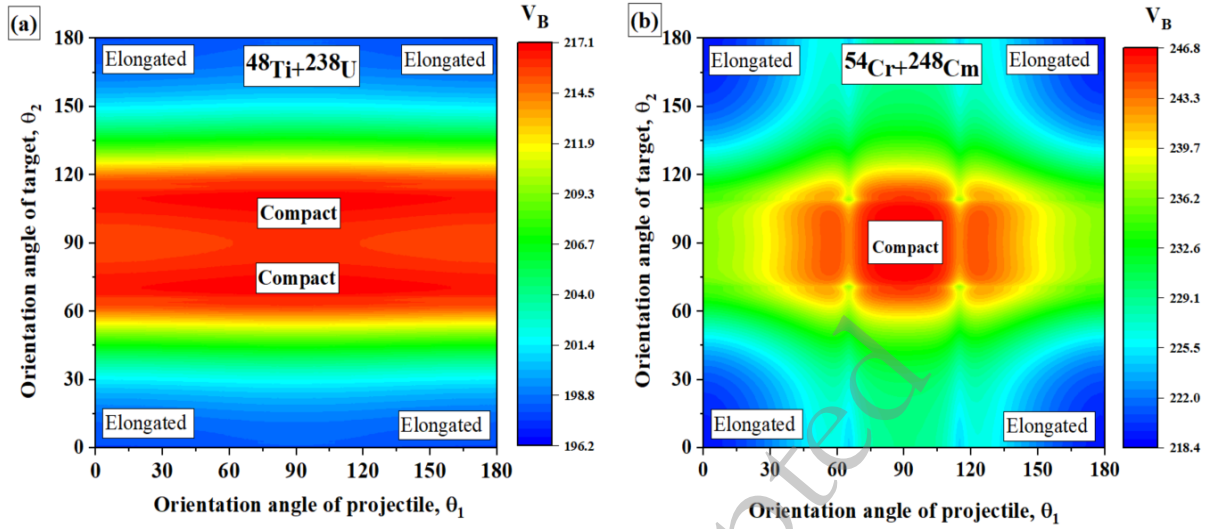


Fig. 7. (color online) Schematic representation of the variation in interaction barrier height as a function of the projectile (θ_1) and target (θ_2) orientation angles for deformed-deformed P-T combinations: (a) $^{48}\text{Ti}+^{238}\text{U}$, and (b) $^{54}\text{Cr}+^{248}\text{Cm}$.

jectile orientation for such a P-T combination would not impose any significant change in the barrier height for both configurations. Meanwhile, for reaction ^{54}Cr ($\beta_2 = 0.161$, $\beta_4 = 0.048$, $\beta_6 = -0.024$) + ^{248}Cm ($\beta_2 = 0.250$, $\beta_4 = 0.039$, $\beta_6 = -0.035$), where both the P-T have significant deformations, the barrier height V_B is sensitive to the orientation angle of both projectile and target nuclei, as shown in Fig. 7(b). While the compact configuration with the highest V_B is observed at $\theta_1, \theta_2 = 90^\circ, 101^\circ$, the elongated configuration with the lowest V_B occurs at $\theta_1, \theta_2 = 180^\circ, 0^\circ$. For this P-T combination, a slight change in the projectile orientation θ_1 can impose a significant change in the barrier height V_B , signifying the influence of projectile orientation θ_1 along with the target orientation θ_2 . These findings point out the possible influence of the projectile deformation on the barrier characteristics of deformed-deformed P-T combinations.

Till now, we discussed the influence of $\beta_2\beta_4\beta_6$ deformations on the barrier characteristics of spherical+deformed and deformed+deformed P-T nuclei, along with their modified compact and elongated configurations. To further examine the role of these configurations on the fusion dynamics of the considered P-T combinations, we study the total interaction potential V_T ($= V_C + V_N$) as a function of the separation distance R for the reaction $^{48}\text{Ti} + ^{238}\text{U}$, shown in Fig. 8. The total interaction potential V_T directly reflects the effect of nuclear deformations and orientations introduced through both the Coulomb potential V_C and nuclear potential V_N . It is worth noting that both the projectile, ^{48}Ti , and the target, ^{238}U , are prolate deformed. The Fig. 8, demonstrates the variation of the V_T for the elongated and compact configurations of the deformed projectile and target (P-T) in comparison to the spherical scenario. Fig. 8(a) represents the case where the projectile nucleus is considered spherical, while Fig. 8(b)

includes the deformation of both projectile and target nuclei. In both cases, the elongated configuration lowers the barrier height V_B compared to the compact and spherical configurations (P-T are spherical), thereby reducing the extra push energy required for fusion. This lowering of the barrier is more pronounced when projectile deformation is taken into account, as seen in Fig. 8(b). These results are due to the modification in the shape of the nuclei by the incorporation of deformations. Consequently, the inclusion of higher-order deformations for both projectile and target nuclei leads to a lowering of the fusion barrier and enhances the probability of fusion at elongated configurations.

So far, the impact of both the magnitude and sign (\pm) of symmetric higher-order deformations (up to β_6) on barrier characteristics, i.e. barrier height (V_B) and barrier position (R_B), has been systematically analysed for both spherical+deformed and deformed+deformed P-T combinations. In further calculations, we have implemented these modified barrier characteristics and their corresponding compact and elongated configurations to determine the capture cross-sections σ_{cap} , which reflect the combined influence of hexacontatetrapole deformations β_6^\pm over a wide range of incident energies $E_{c.m.}$, spanning across the Coulomb barrier.

C. Capture cross-sections for spherical + deformed and deformed+deformed projectile-target

In this section, the relevance of the obtained modified barrier characteristics and their corresponding compact and elongated configurations for both spherical+deformed and deformed+deformed projectile-target (P-T) combinations is exercised to calculate the capture cross-sections. The capture cross-sections (σ_{cap}) are obtained using the ℓ -summed Wong model for the center of mass

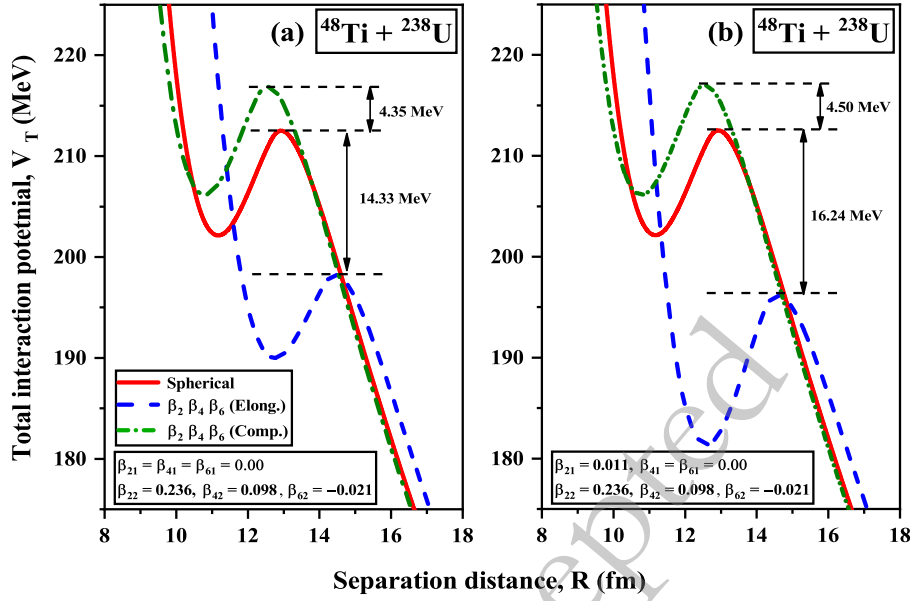


Fig. 8. (color online) Total interaction potential V_T (MeV) is represented as a function of separation distance R (fm) for the P-T combination of (a) ^{48}Ti ($\beta_{21} = \beta_{41} = \beta_{61} = 0.00$) + ^{238}U ($\beta_{22} = 0.236, \beta_{42} = 0.098, \beta_{62} = -0.021$) and (b) ^{48}Ti ($\beta_{21} = 0.011, \beta_{41} = \beta_{61} = 0.00$) + ^{238}U ($\beta_{22} = 0.236, \beta_{42} = 0.098, \beta_{62} = -0.021$). The variations of V_T and R are illustrated for both elongated and compact configurations of the deformed nuclei, along with the case where both projectile and target are considered spherical (red line).

energies $E_{c.m.}$ lying across the Coulomb barrier. Initially, the σ_{cap} for P-T combination $^{48}\text{Ca} + ^{244}\text{Pu}$ are calculated using β_4 and β_6 deformed nuclei at their respective elongated and compact configurations in comparison to the available experimental data [51], as shown in Fig.9. This figure illustrates the variation in the σ_{cap} for the reaction under consideration at their optimum as well as integrated orientations across a range of $E_{c.m.}$. One can observe that the elongated configuration yields an enhanced σ_{cap} compared to that of the compact configuration for both $\beta_2\beta_4$ and $\beta_2\beta_4\beta_6$ deformations. This difference is attributed to the lower V_B for capture at the elongated configuration, which is associated with the shape modifications induced by these deformations. Also, the calculated integrated cross-sections reflect the average effect of the cross-sections obtained at various orientations, which lie between the compact and elongated configurations. As the elongated configuration yields better agreement with experimental data, therefore, the σ_{cap} are calculated at their elongated configuration for all considered P-T combinations involving ^{48}Ca induced reactions with ^{238}U and ^{248}Cm , as well as ^{36}S and ^{48}Ti induced reactions with ^{238}U . The obtained σ_{cap} values corresponding to both configurations are compared with available experimental data, as shown in Fig.10. However, the reactions depicted in Fig.10(a,d) exhibit center of mass energies $E_{c.m.}$ lying above the barrier, beyond the V_B corresponding to the elongated configuration for both β_4 and β_6 deformations; thus aligning well with the experimental cross-sections. For the reaction involving $^{48}\text{Ca} + ^{238}\text{U}$, the presence of β_6^- in ^{238}U induces the hindrance to σ_{cap} for energies $E_{c.m.}$ ly-

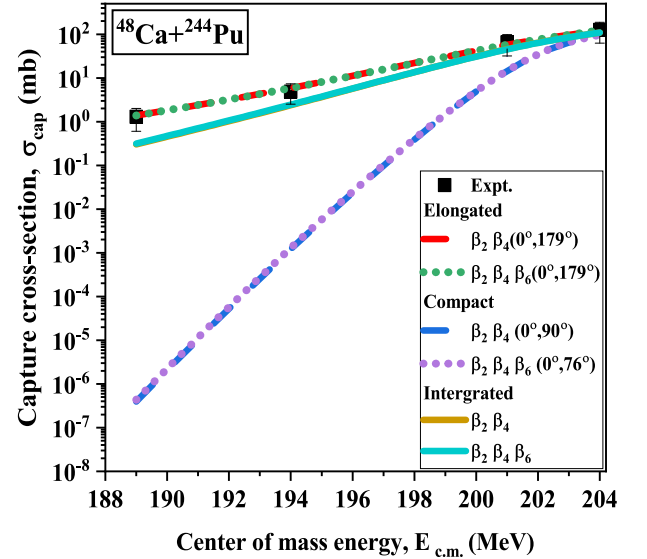


Fig. 9. (color online) Schematic diagram of Capture cross-sections (σ_{cap}) calculated using ℓ -summed Wong model as a function of $E_{c.m.}$ at compact and elongated configurations of $\beta_2\beta_4$ and $\beta_2\beta_4\beta_6$ along with the cross-sections integrated over all orientations for reaction $^{48}\text{Ca} + ^{244}\text{Pu}$.

ing below and near the Coulomb barrier, due to increased V_B in comparison to β_4^+ case as shown in Fig.10(b). Meanwhile, the presence of the deformed projectile ^{36}S with β_6^- deformation leads to an enhancement of the capture cross-sections compared to the case with β_4 deformation alone [Fig.10(c)]. Furthermore, the integrated capture cross-sections hold significant value in light of ex-

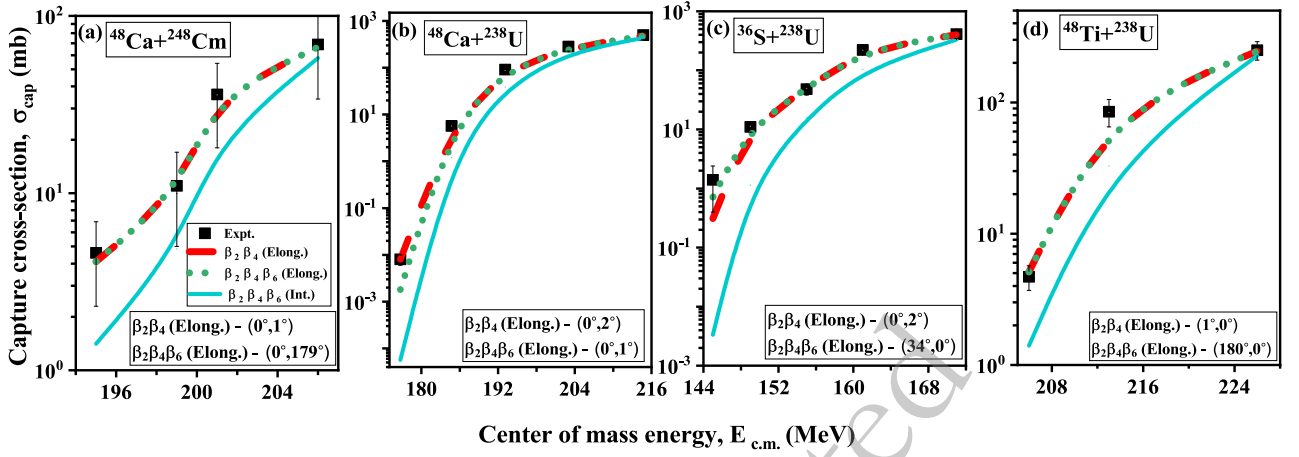


Fig. 10. (color online) Schematic diagram of Capture cross-sections (σ_{cap}) obtained using ℓ -summed Wong model as a function of $E_{c.m.}$ at elongated configurations and integrated over all orientations of $\beta_2\beta_4$ and $\beta_2\beta_4\beta_6$ for considered P-T combinations, then compared with available experimental data.

perimental studies. However, the integrated cross-sections calculated for these considered reactions, which account for the averaged contributions from all P–T orientations, exhibit a suppression relative to those obtained for the elongated configurations, as shown in Fig.10. To address this suppression and to determine the relevance of all orientations of $\beta_2\beta_4\beta_6$ through integrated cross-sections from an experimental perspective, we explored the σ_{cap} using the Wong Model. The obtained results are compared with experimental cross-sections as well as σ_{cap} calculated at the elongated configuration using the ℓ -summed Wong Model for the reaction $^{48}\text{Ca}+^{238}\text{U}$, as illustrated in Fig.11. The analysis reveals that the integrated

cross-sections derived from the Wong Model offer a decent agreement with experimental data as we incorporate deformation up to β_6 , while the integrated cross-sections from the ℓ -summed Wong Model are notably suppressed as partial waves are included up to ℓ_{max} only. Thus, leading to the conclusion that the inclusion of β_6 alongside $\beta_2\beta_4$ can significantly affect σ_{cap} at elongated configuration and integrated orientations.

The considered reactions have experimental data available for energies lying above the barrier. To quantify the impact of β_6^\pm relative to β_4^\pm , we evaluate the capture cross-sections for the reaction $^{48}\text{Ca}+^{246}\text{Es}$ forming the CN with $Z=119$ at centre-of-mass energies ($E_{c.m.}$) ran-

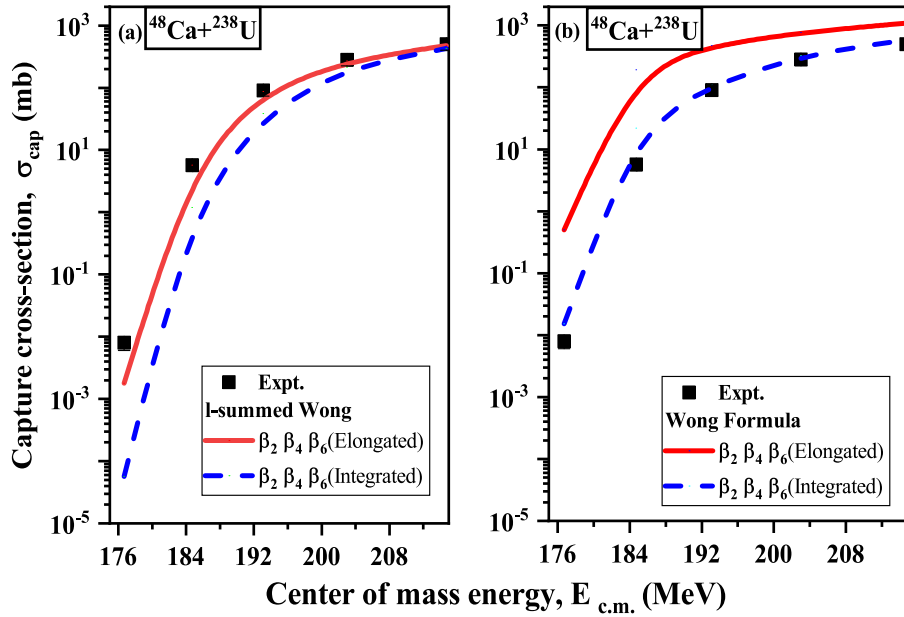


Fig. 11. (color online) Schematic representation of capture cross-sections (σ_{cap}) calculated using (a) ℓ -summed Wong model and (b) Wong Model as a function of $E_{c.m.}$. Results are shown for elongated configurations as well as integrated calculations for $\beta_2\beta_4\beta_6$ deformed case, and compared with the available experimental data for the considered P–T combination of $^{48}\text{Ca}+^{238}\text{U}$.

ging from 180 to 220 MeV, spanning across the barrier. These capture cross-sections are calculated using the Wong formula at the elongated configurations and integrated cross-sections of all the orientations of P-T of $\beta_2\beta_4$ and $\beta_2\beta_4\beta_6$ with both positive and negative signs. As seen in Fig.12(a), incorporating β_6^+ into $\beta_2^+\beta_4^+$ markedly enhances σ_{cap} , whereas β_6^- introduces a noticeable suppression. Conversely, in Fig.12(b), the σ_{cap} for the $\beta_2^+\beta_4^-$ deformation, when β_6^+ is present, is enhanced due to variation in the V_B resulting from the shape modification in $\beta_2^+\beta_4^-\beta_6^+$ case as discussed in the preceding section. On the other hand, the integrated cross-sections follow a similar trend to the elongated configurations upon the inclusion of $\beta_2^+\beta_4^-\beta_6^+$ deformations, though they show suppression comparatively to elongated configurations, as illustrated in Fig.12 and discussed in the previous paragraph. Furthermore, according to the analysis presented in [11, 66] regarding the synthesis of superheavy nuclei (SHN) with $Z=120$, the combination of ^{50}Ti and ^{249}Cf as projectile and target is identified as the most favourable for achieving SHN with $Z=120$. Consequently, the estimated capture cross-sections are derived using Wong's formula, which incorporates higher-order deformations $\beta_2\beta_4$ and $\beta_2\beta_4\beta_6$ at their elongated and integrated cross-sections, as a function of the range of center of mass energies that lie across the Coulomb barrier, as depicted in Fig.12 (c). From this figure, it is evident that the addition of β_6^- in conjunction with β_2^+ and β_4^+ results in a reduction of the cross-sections in both configurations when compared to the scenario involving solely $\beta_2^+\beta_4^+$. Nevertheless, this reduction is less significant in the integrated configuration, due to the collective effects from all orientations.

Furthermore, we have incorporated a comprehensive

comparison of our calculated results with those derived from the microscopic Time-Dependent Hartree-Fock (TDHF) method. This comparison is illustrated in the Fig.13. In this Figure, we depict the capture cross-sections (σ_{cap}) calculated using the ℓ -summed Wong model and compare them with results from the Density-Constrained Frozen Hartree-Fock (DC-FHF) potential within the TDHF framework [67], alongside experimental data from [68] available for the reaction $^{48}\text{Ca} + ^{238}\text{U}$ forming the compound nucleus ^{286}Cn . This recent TDHF-based study is particularly important as it investigates the influence of higher-order deformations ($\beta_2, \beta_4, \beta_6$) and their orientation effects on the capture dynamics. Therefore, this work is chosen for comparison and analysis in our study. The results of Fig.13 indicate that cross-sections obtained with the ℓ -summed Wong model for the elongated configuration are in closer agreement with the experimental data compared to the integrated cross-sections σ_{cap} , as well as the integrated and elongated cross-sections obtained from the TDHF calculations.

Overall, these findings underscore the crucial role of higher-order β_6 deformations, alongside β_2 and β_4 , in modifying barrier characteristics and capture cross-sections in heavy-ion reactions that lead to the formation of superheavy nuclei.

IV. SUMMARY

The present work offers a deep insight into the higher-order deformations (up to hexacontatetrapole deformations β_6) and their corresponding orientations on the synthesis of superheavy nuclei (SHN). The analysis provides an explicit role of different signs and magnitudes of β_6 on

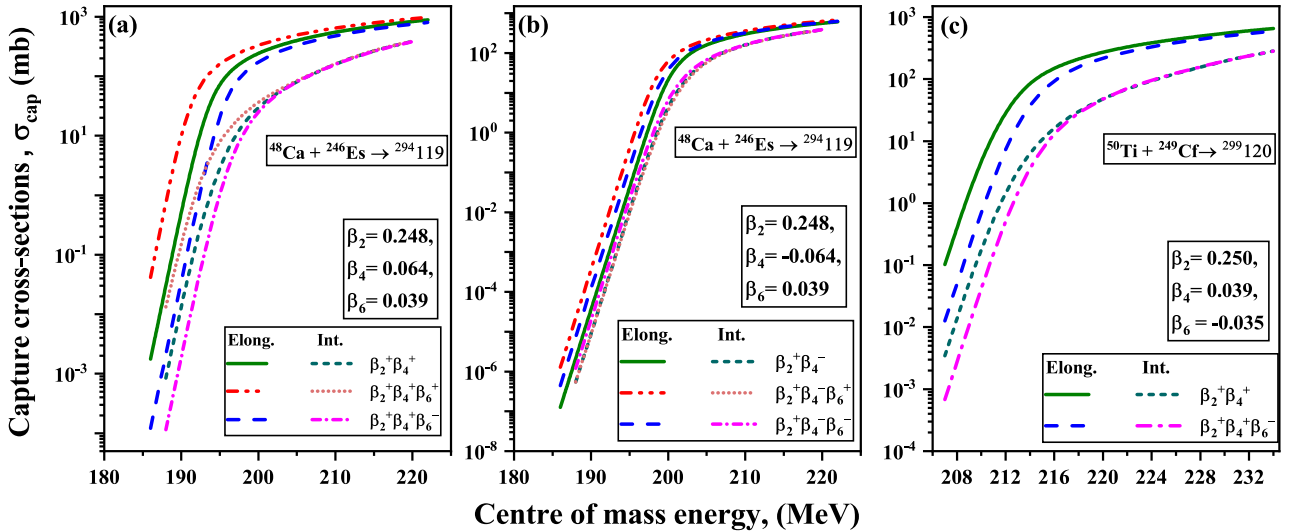


Fig. 12. (color online) Schematic diagram of Capture cross-sections (σ_{cap}) as a function of center-of-mass energy for the reaction (a) $^{48}\text{Ca} + ^{246}\text{Es}$ ($Z=119$) with $\beta_2^+\beta_4^+$, $\beta_2^+\beta_4^-\beta_6^+$ combinations, (b) $^{48}\text{Ca} + ^{246}\text{Es}$ ($Z=119$) with $\beta_2^+\beta_4^-$, $\beta_2^+\beta_4^-\beta_6^+$ combinations, (c) $^{50}\text{Ti} + ^{249}\text{Cf}$ ($Z=120$) calculated using the Wong's formula. The results are shown for combinations of the deformations considered at their elongated configuration and integrated cross-section over all orientations.

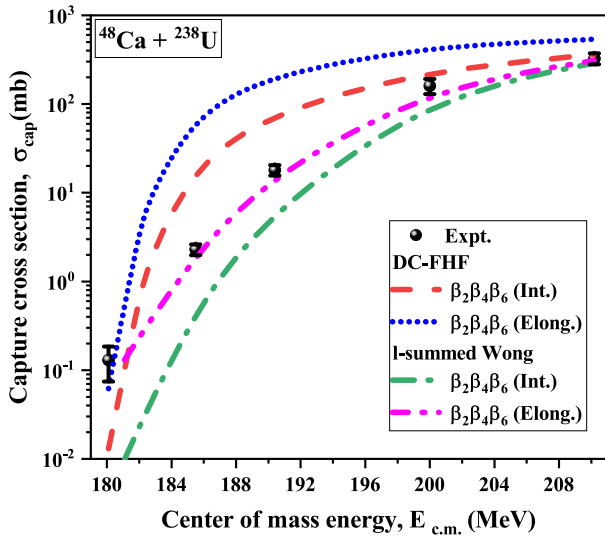


Fig. 13. (color online) Schematic representation of the capture cross-sections (σ_{cap}) obtained from the ℓ -summed Wong model as a function of the center-of-mass energy (E_{cm}) for the reaction $^{48}\text{Ca} + ^{238}\text{U}$, evaluated at elongated configurations and integrated over all orientations for deformations $\beta_2\beta_4\beta_6$. The calculated results are compared with the corresponding experimental data and with σ_{cap} values extracted from the DC-FHF model at both configurations.

the heavy-ion induced reactions in conjunction with quadrupole (β_2) and hexadecapole (β_4) deformations of the target nuclei. We consider the P-T combinations $^{48}\text{Ca} + ^{248}\text{Cm}$, $^{48}\text{Ca} + ^{244}\text{Pu}$, $^{48}\text{Ca} + ^{238}\text{U}$, $^{36}\text{S} + ^{238}\text{U}$ and $^{48}\text{Ti} + ^{238}\text{U}$ leading to the formation of SHN ^{296}Lv , ^{292}Fl , ^{286}Cn , ^{274}Hs and ^{286}Fl . The shape evolution of the deformed actinide target nuclei due to incorporation of these deformations alters the barrier characteristics, i.e.,

the barrier height V_B and barrier position R_B of the interactions influencing the formation of the SHN, with variations depending on the sign of β_6^\pm . For instance, incorporation of β_6^+ leads to simultaneous elongation along the poles and compression at the belly, whereas incorporation of β_6^- leads to elongation at the belly and compression along the poles in the $\beta_2^+\beta_4^+$ deformed nuclei. The influence of β_6 is further analyzed for three magnitude relations: (a) $\beta_4 > \beta_6$, (b) $\beta_4 \approx \beta_6$, and (c) $\beta_4 < \beta_6$ respectively. The analysis indicates notable differences in the barrier characteristics for the elongated configuration, while no such differences are observed for the compact configuration, shifting the focus towards the elongated configuration, considering various combinations of $\beta_2, \beta_4, \beta_6$ deformations. The findings indicate that the incorporation of β_6^+ deformation lowers the V_B , whereas the incorporation of β_6^- increases the V_B when integrated with $\beta_2^+\beta_4^+$ deformation for the cases where $\beta_4 \approx \beta_6$ and $\beta_4 < \beta_6$. These results are in agreement with the previously defined behaviour of β_4^+ deformed nuclei. However, for the cases with $\beta_4 > \beta_6$, deviations from this trend are observed in $\beta_2^+\beta_4^+\beta_6^\pm$ deformed nuclei due to the predominance of β_4 over β_6 . The possible influence of the orientation of the deformed projectile nuclei has also been discussed. These modified barrier characteristics are then utilized to calculate the capture cross-sections for the considered P-T combinations, showing better agreement with available experimental data at elongated configurations, for the synthesis of SHE. While the above-mentioned results provide significant understanding of the reaction dynamics of the nuclei involving β_2, β_4 , and β_6 deformations having the axially symmetric shape, it will be of future interest to investigate the relevance of octupole (β_3) deformations where reflection asymmetry becomes significant.

References

- [1] S. Hofmann, *J. Nucl. Radiochem. Sci.* **4**, R1 (2003)
- [2] Y. Abe, Y. Aritomo, *et al.*, *J. Phys. G: Nucl. Part. Phys.* **23**, 1275 (1997)
- [3] V. L. Litnensky, V. V. Pashkevich, *et al.*, *Phys. Rev. C* **89**, 034626 (2014)
- [4] C. Shen, G. Kosenko, and Y. Abe, *Phys. Rev. C* **66**, 061602 (2002)
- [5] V. Volkov, G. Adamian, *et al.*, *Phys. Atom. Nuclei* **64**, 1116 (2001)
- [6] S. Chopra, Hemdeep, and R. K. Gupta, *Phys. Rev. C* **95**, 044603 (2017)
- [7] Y. T. Oganessian and V. K. Utyonkov, *Rep. Prog. Phys.* **78**, 036301 (2015)
- [8] C. Jiang, B. Back, K. Rehm, *et al.*, *Eur. Phys. J. A* **57**, 235 (2021)
- [9] O. R. Smits, C. E. Düllmann, *et al.*, *Nat. Rev. Phys.* **6**, 86 (2024)
- [10] G. Montagnoli and A. Stefanini, *Eur. Phys. J. A* **59**, 138 (2023)
- [11] S. Rana, R. Kumar, and M. Bhuyan, *Phys. Rev. C* **104**, 024619 (2021)
- [12] B. B. Back, H. Esbensen, *et al.*, *Rev. Mod. Phys.* **86**, 317 (2014)
- [13] A. S. Umar, V. E. Oberacker, *et al.*, *Phys. Rev. C* **81**, 064607 (2010)
- [14] Z.-Q. Feng, G.-M. Jin, J.-Q. Li, and W. Scheid, *Nucl. Phys. A* **816**, 33 (2009)
- [15] W. Reisdorf and M. Schdel, *Z. Physik A - Hadrons and Nuclei* **343**, 47 (1992)
- [16] M. Beckerman, *Rep. Prog. Phys.* **51**, 1047 (1988)
- [17] S. Jain, M. K. Sharma, and R. Kumar, *Chin. Phys. C* **46**, 014102 (2022)
- [18] S. Mitsuoka, H. Ikezoe, K. Nishio, and J. Lu, *Phys. Rev. C* **62**, 054603 (2000)
- [19] V. A. B. Zagatto, C. E. Aguiar, J. Lubian, and L. F. Canto, *Phys. Rev. C* **111**, 024617 (2025)
- [20] M. S. Gautam, *Mod. Phys. Lett. A* **30**, 1550013 (2015)
- [21] M. Gautam, *Indian J. Phys.* **90**, 335 (2016)
- [22] A. Nasirov, A. Fukushima, *et al.*, *Nucl. Phys. A* **759**, 342 (2005)

- [23] L. Zhu, Z.-Q. Feng, C. Li, and F.-S. Zhang, *Phys. Rev. C* **90**, 014612 (2014)
- [24] M. Kaur, M. K. Sharma, and R. K. Gupta, *Phys. Rev. C* **86**, 064610 (2012)
- [25] V. V. Sargsyan, G. G. Adamian, *et al.*, *Phys. Rev. C* **85**, 037602 (2012)
- [26] G. Fazio, G. Giardina, *et al.*, *Journal of the Physical Society of Japan* **72**, 2509 (2003)
- [27] K. Kim, Y. Kim, *et al.*, *Phys. Rev. C* **91**, 064608 (2015)
- [28] R. A. Kuzyakin, V. V. Sargsyan, *et al.*, *Phys. Rev. C* **92**, 014603 (2015)
- [29] R. K. Gupta, M. Balasubramanian, *et al.*, *Journal of Physics G: Nuclear and Particle Physics* **31**, 631 (2005)
- [30] V. Y. Denisov and N. A. Pilipenko, *Phys. Rev. C* **76**, 014602 (2007)
- [31] V. Y. Denisov and N. A. Pilipenko, *Phys. Rev. C* **81**, 025805 (2010)
- [32] N. Jain, M. Bhuyan, and R. Kumar, *Phys. Rev. C* **109**, 034617 (2024)
- [33] S. Rana, M. Bhuyan, R. Kumar, and B. V. Carlson, *Phys. Rev. C* **110**, 024601 (2024)
- [34] H. Sharma, S. Jain, R. Kumar, *et al.*, *Phys. Rev. C* **108**, 044613 (2023)
- [35] S. Jain, M. K. Sharma, and R. Kumar, *Phys. Rev. C* **101**, 051601 (2020)
- [36] H. Sharma, S. Jain, R. Kumar, *et al.*, *Eur. Phys. J. A* **59** (2023).
- [37] M. Ismail, W. Seif, and M. Botros, *Nucl. Phys. A* **828**, 333 (2009)
- [38] M. Manhas, R. K. Gupta, *et al.*, *Phys. Rev. C* **74**, 034603 (2006)
- [39] D. L. Hendrie, B. G. Harvey, *et al.*, *Phys. Rev. Lett.* **30**, 571 (1973)
- [40] J. M. Moss, Y. D. Terrien, *et al.*, *Phys. Rev. Lett.* **26**, 1488 (1971)
- [41] G. Pálla, H. Geramb, and C. Pegel, *Nucl. Phys. A* **403**, 134 (1983)
- [42] C. R. Morton, A. C. Berriman, *et al.*, *Phys. Rev. C* **64**, 034604 (2001)
- [43] T. Rumin, K. Hagino, and N. Takigawa, *Phys. Rev. C* **61**, 014605 (1999)
- [44] A. Iwamoto, P. Möller, *et al.*, *Nucl. Phys. A* **596**, 329 (1996)
- [45] V. E. Oberacker, M. Seiwert, and W. Greiner, *Z. Phys. A - Atoms and Nuclei* **310** (1983), 10.1007/BF01419514.
- [46] R. K. Gupta, M. Manhas, and W. Greiner, *Phys. Rev. C* **73**, 054307 (2006)
- [47] D. Jain, R. Kumar, and M. K. Sharma, *Nucl. Phys. A* **915**, 106 (2013)
- [48] R. Kumar, M. K. Sharma, and R. K. Gupta, *Nucl. Phys. A* **870-871**, 42 (2011)
- [49] R. Kumar, *Phys. Rev. C* **84**, 044613 (2011)
- [50] P. Möller, A. J. Sierk, *et al.*, *At. Data Nucl. Data Tables* **109**, 1 (2016)
- [51] G. Itkis, M.G. and Knyazheva, I. Itkis, *et al.*, *Eur. Phys. J. A* **58** (2022).
- [52] J. P. Davidson, *Rev. Mod. Phys.* **37**, 105 (1965)
- [53] R. S. Mackintosh, *Rep. Prog. Phys.* **40**, 731 (1977)
- [54] J. Blocki, J. Randrup, *et al.*, *Ann. Phys. (NY)* **105**, 427 (1977)
- [55] R. Kumar, M. Bansal, *et al.*, *Phys. Rev. C* **80**, 034618 (2009)
- [56] R. K. Gupta, N. Singh, and M. Manhas, *Phys. Rev. C* **70**, 034608 (2004)
- [57] M. Seiwert, W. Greiner, *et al.*, *Phys. Rev. C* **29**, 477 (1984)
- [58] N. Malhotra and R. K. Gupta, *Phys. Rev. C* **31**, 1179 (1985)
- [59] C. Y. Wong, *Phys. Rev. Lett.* **31**, 766 (1973)
- [60] Z. Gao-Long, L. Xiao-Yun, and L. Zu-Hua, *Chin. Phys. Lett.* **25**, 1247 (2008)
- [61] R. Bass, *Nucl. Phys. A* **231**, 45 (1974)
- [62] W. Swiatecki, *Nucl. Phys. A* **376**, 275 (1982)
- [63] N. Wang, J. Chen, Y. Wang, and H. Yao, *Phys. Rev. C* **111**, 024621 (2025)
- [64] W. Scobel, H. H. Gutbrod, *et al.*, *Phys. Rev. C* **14**, 1808 (1976)
- [65] D. L. Hill and J. A. Wheeler, *Phys. Rev.* **89**, 1102 (1953)
- [66] H. Albers, J. Khuyagbaatar, D. Hinde, *et al.*, *Physics Letters B* **808**, 135626 (2020)
- [67] X.-X. Sun and L. Guo, *Phys. Rev. C* **107**, 064609 (2023)
- [68] K. Nishio, S. Mitsuoka, *et al.*, *Phys. Rev. C* **86**, 034608 (2012)